

# Robust and Generalizable Atrial Fibrillation Detection from ECG Using Time-Frequency Fusion and Supervised Contrastive Learning

**Hongtao Li<sup>1</sup>, Jia Wei<sup>3</sup>, Jia Xiao<sup>2</sup>, Yuanjun Lai<sup>2</sup>, Mingyang Liu<sup>3</sup>, Shuzhen Lv<sup>2</sup>, and Xueqiang Ouyang<sup>2,\*</sup>**

<sup>1</sup>The People's Hospital of Baoan Shenzhen, Shenzhen 518101, Guangdong, China

<sup>2</sup>Information Center, The People's Hospital of Baoan Shenzhen, Shenzhen 518101, Guangdong, China

<sup>3</sup>School of Computer Science and Engineering, South China University of Technology, Guangzhou 510006, Guangdong, China

\*corresponding: xqoy.bahosp@outlook.com

## ABSTRACT

Atrial fibrillation (AF) is a common cardiac arrhythmia that significantly increases the risk of stroke and heart failure, necessitating reliable and generalizable detection methods from electrocardiogram (ECG) recordings. Although deep learning has advanced automated AF diagnosis, existing approaches often struggle to exploit complementary time–frequency information effectively, limiting both robustness under intra-dataset and generalization across diverse clinical datasets. To address these challenges, we propose a cross-modal deep learning framework comprising two key components: a Bidirectional Gating Module (BGM) and a Cross-modal Supervised Contrastive Learning (CSCL) strategy. The BGM facilitates dynamic, reciprocal refinement between time- and frequency-domain features, enhancing model robustness to signal variations within a dataset. Meanwhile, CSCL explicitly structures the joint embedding space by pulling together label-consistent samples and pushing apart different ones, thereby improving inter-class separability and enabling strong cross-dataset generalization. We evaluate our method through five-fold cross-validation on the AFDB and the CPSC2021 dataset, as well as bidirectional cross-dataset experiments (training on one and testing on the other). Results show consistent improvements over state-of-the-art methods across multiple metrics, demonstrating that our approach achieves both high intra-dataset robustness and excellent cross-dataset generalization. We further demonstrate that our method achieves high computational efficiency and anti-interference capability, making it suitable for edge deployment.

## Introduction

Atrial fibrillation (AF) is the most prevalent cardiac arrhythmia worldwide, affecting more than 50 million individuals—a number projected to increase with population aging—and imposes a substantial and growing burden on healthcare systems<sup>1</sup>. AF markedly increases the risk of ischemic stroke and is associated with heart failure, cognitive impairment, and increased all-cause mortality<sup>2</sup>. Approximately 27% cases of AF are asymptomatic or paroxysmal, often escaping detection during routine clinical screening<sup>3</sup>. This diagnostic gap highlights the critical need for automated AF detection systems that combine high sensitivity and specificity to enable timely intervention and prevent severe complications.

The electrocardiogram (ECG) provides the main basis for AF diagnosis, offering detailed electrophysiological information<sup>4</sup>. In clinical practice, ECG assessments are typically performed using standard 12-lead recordings or ambulatory Holter monitoring. A standard 12-lead ECG captures a short (approximately 10-second) segment of cardiac activity and can confirm AF when characteristic features, such as absent P-waves, irregular f-waves, and an irregular R–R interval, are present<sup>5</sup>. However, its short duration limits its effectiveness for detecting paroxysmal AF, which occurs intermittently and unpredictably. Holter monitoring addresses this limitation by enabling continuous ECG recording over 24 hours to 7 days through portable devices, making it the preferred method for evaluating suspected paroxysmal AF when standard ECG results are negative<sup>6</sup>. Despite its extended observation window, Holter analysis traditionally depends on manual review, which is labor-intensive, prone to inter-observer variability, and unsuitable for large-scale or real-time applications<sup>7</sup>.

Recent advances in machine learning and deep learning have facilitated automated detection of AF from ECG signals<sup>8</sup>. However, the majority existing methods rely on features extracted from a single signal domain (either time or frequency) and consequently overlook the complementary electrophysiological characteristics of AF. Clinically, AF manifests through two interrelated patterns: an irregular ventricular response in the time domain and spectrally diffuse atrial activity in the frequency domain<sup>9</sup>. Models confined to one domain capture only a partial view of this arrhythmia, which compromises their robustness

and generalizable under real-world recording variability.

A further limitation lies in how multimodal information is integrated and learned. Conventional fusion strategies—such as simple concatenation or fixed-weight averaging—process time- and frequency-domain features independently, ignoring their context-dependent interactions<sup>10</sup>. At the same time, representation learning without explicit supervision often yields embeddings with insufficient class separation, particularly in the presence of noisy. These issues not only limit performance within a given dataset but also hinder model transfer across diverse clinical datasets<sup>11</sup>.

To address these challenges, we propose **MGCNet (Multimodal Gated Contrastive Network)**, a deep learning architecture for robust and generalizable AF detection from ambulatory ECG recordings. Our approach delivers three key contributions:

(1) A **Bidirectional Gating Module (BGM)** that enables dynamic, reciprocal refinement between temporal and spectral features. By allowing each modality to adaptively modulate the other based on contextual relevance, BGM enhances resilience to intra-dataset variations such as noise and morphological diversity, thereby improving robustness.

(2) A **Cross-modal Supervised Contrastive Learning (CSCL)** strategy that explicitly structures the joint embedding space by pulling together same-class samples and pushing apart different-class samples. This promotes semantic consistency and mitigates dataset-specific biases, leading to strong cross-dataset generalization.

(3) State-of-the-art performance on two widely used benchmarks: comprehensive evaluation on the CPSC2021 and AFDB demonstrates that MGCNet consistently outperforms existing methods across multiple metrics under both intra-dataset and cross-dataset settings, confirming its effectiveness and practical applicability.

## Related Works

Research on automatic AF detection has undergone a paradigm shift—from rule-based and traditional machine learning approaches to end-to-end deep learning frameworks. Early methods relied heavily on expert-designed features and shallow classifiers, whereas recent advances leverage deep neural networks to learn direct representation from raw or transformed signals<sup>12</sup>.

Traditional AF detection methods relied on handcrafted features, such as RR interval statistics and time–frequency descriptors, to capture AF’s characteristic rhythm irregularity and spectral disorganization, combined with classical classifiers like SVM, random forests, or k-NN<sup>1314</sup>. While effective on clean, controlled datasets, these approaches were inherently limited by manual feature design and often generalized poorly across diverse devices, patient cohorts, and real-world noise conditions.

The rise of deep learning has shifted AF detection toward end-to-end models that learn directly from ECG signals without relying on handcrafted features. Initial deep learning approaches operated primarily in the time domain. For example, Xia et al.<sup>15</sup> applied one-dimensional convolutional neural networks (1D-CNNs) to raw ECG waveforms, demonstrating the feasibility of data-driven rhythm classification. Later work incorporated recurrent networks<sup>1617</sup> and Transformer architectures<sup>1819</sup> to better model long-range temporal dependencies, while others introduced multi-scale convolutions<sup>2021</sup> or attention mechanisms<sup>22</sup> to enhance local and global feature extraction. Li et al.<sup>23</sup> took a different route by reshaping 1D ECG segments into a 2D “Z-shaped” layout to take advantage of image-based CNNs.

At the same time, a parallel line of research focused on the frequency domain. These methods first transformed ECG signals into time–frequency representations, such as short-time Fourier transform (STFT) spectrograms or continuous wavelet scalograms, and then applied 2D-CNNs for classification<sup>242526</sup>. Others explored nonlinear dynamics–based visualizations: for instance, Zhu et al.<sup>27</sup> converted ECG time series into recurrence plots (RPs), which encode temporal self-similarity, and used a ResNet<sup>28</sup> architecture to extract discriminative features for AF detection.

Time- and frequency-domain models have performed well on standard AF detection benchmarks, but each only captures part of the full view: irregular heartbeat timing in the time domain and chaotic atrial activity in the frequency domain. To get a more complete view, recent studies started combining both types of information using multimodal networks that process raw ECG signals together with spectral maps or RR intervals<sup>2930</sup>.

While recent multimodal methods combine time- and frequency-domain features, they often rely on static fusion and standard classification losses, limiting their robustness to signal variations and generalization across datasets. Although contrastive learning has shown promise in medical representation learning<sup>3132</sup>, none explicitly align temporal and spectral embeddings under a unified supervised objective. Our MGCNet addresses this by jointly modeling dynamic cross-modal interaction and discriminative feature learning—directly enhancing both robustness and generalization in AF detection.

## Materials and Methods

### Materials

We utilize two publicly available ECG databases for AF analysis: the MIT-BIH Atrial Fibrillation Database (AFDB) and the China Physiological Signal Challenge 2021 (CPSC2021). The AFDB<sup>33</sup> consists of 25 long-term ECG recordings from patients with documented AF. Among them, 23 records contain two simultaneously recorded ECG signals along with expert-annotated

rhythm labels. Records 00735 and 03665 are excluded due to the absence of annotations. Each recording lasts approximately 10 hours, sampled at 250 Hz. The **CPSC2021** dataset<sup>34</sup> provides variable-length ECG segments extracted from Lead I and Lead II of long-term Holter recordings, sampled at 200 Hz. The data are released in two phases: Phase I includes 730 recordings from 12 AF patients and 42 non-AF patients; Phase II includes 706 recordings from 37 AF patients and 14 non-AF patients. In total, the dataset comprises 1,436 recordings from 105 unique patients.

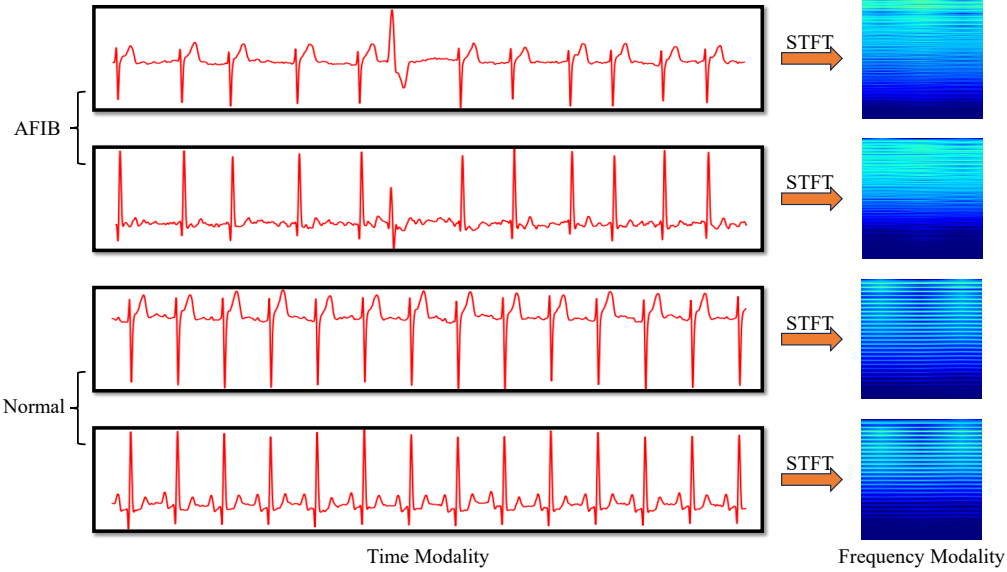


**Figure 1.** Spectrogram of the cleaned ECG segment generated via STFT, encoded as a three-channel heatmap for frequency-domain modeling. In the time domain, AFIB is characterized by the absence of P waves and highly irregular R-R intervals. In the frequency domain (STFT spectrogram), it exhibits a diffuse and chaotic spectral pattern.

All ECG recordings from the AFDB and the CPSC2021 are uniformly resampled to 250 Hz, and only the first lead is retained. The preprocessing pipeline consists of four sequential steps:

**Filtering.** To suppress baseline wander, powerline interference, and high-frequency noise, each raw ECG signal  $x[n]$  is filtered using a zero-phase fourth-order Butterworth bandpass filter with cutoff frequencies of 0.5 Hz and 40 Hz<sup>35</sup>. The filtering is implemented in forward–backward mode to eliminate phase distortion:

$$x_{\text{clean}}[n] = \text{filtfilt}(b_{\text{BP}}, a_{\text{BP}}, x[n]), \quad (1)$$

where  $b_{\text{BP}}$  and  $a_{\text{BP}}$  are the numerator and denominator coefficients of the discrete-time bandpass filter, obtained by cascading a low-pass section ( $f_c = 40$  Hz) and a high-pass section ( $f_c = 0.5$  Hz). This preserves the morphological integrity of the P-wave, QRS complex, and T-wave while attenuating out-of-band artifacts.

**Segmentation.** The filtered recording is partitioned into non-overlapping 10-second segments<sup>36</sup>, each containing  $N = 2500$  samples (since  $10 \text{ s} \times 250 \text{ Hz} = 2500$ ). Each segment inherits the original label, resulting in a binary classification task between atrial fibrillation (AFIB) and normal sinus rhythm (N).

**Quality Assessment.** To avoid misleading the model with noisy or artifact-contaminated segments, we apply an automated quality assessment based on the method of Zhao et al.<sup>3738</sup>. This approach evaluates both R-peak consistency and ECG waveform morphology to assign a binary label ("qualified" or "unqualified"). Only qualified segments are retained for training and evaluation, ensuring that the model learns from physiologically plausible signals and improving its robustness and generalization in real-world scenarios.

**Frequency-Domain Modality Generation.** For each 10-s ECG segment  $x_{\text{clean}}[n] \in \mathbb{R}^{2500}$ , we compute a magnitude spectrogram via short-time Fourier transform (STFT)<sup>39</sup> using a 1-s Hann window ( $N_{\text{win}} = 250$ ) and 50% overlap ( $H = 125$ ) at 250 Hz sampling rate. To emphasize physiologically relevant dynamics while suppressing noise, we retain frequencies  $\leq 40$  Hz—beyond which ECG energy is negligible. The spectrogram  $A[m, k] = |X[m, k]|$  is converted to decibels:

$$A_{\text{dB}} = 20 \log_{10}(A + \epsilon), \quad \epsilon = 10^{-8}, \quad (2)$$

clipped to  $[-80, \max(A_{\text{dB}})]$ , and linearly normalized to  $[0, 1]$ . It is then resized to  $128 \times 128$  via anti-aliased bilinear interpolation and mapped to an RGB image using the jet colormap:

$$\mathbf{I}_{\text{freq}} = \text{Colormap}_{\text{jet}}(\tilde{A}) \in [0, 1]^{128 \times 128 \times 3}. \quad (3)$$

This representation preserves AF-associated spectral disorganization and serves as input to the spectral branch of our network (Figure 1).

The final dataset statistics after preprocessing are summarized in Table 1.

**Table 1.** Summary of the AFDB and CPSC2021 datasets used in this study.

Attributes	AFDB	CPSC2021
Number of patients	23	105
Sampling frequency (Hz)	250	200
Number of segments	58771	137010
Number of 'N' segments	36718	89570
Number of 'AFIB' segments	22053	47440

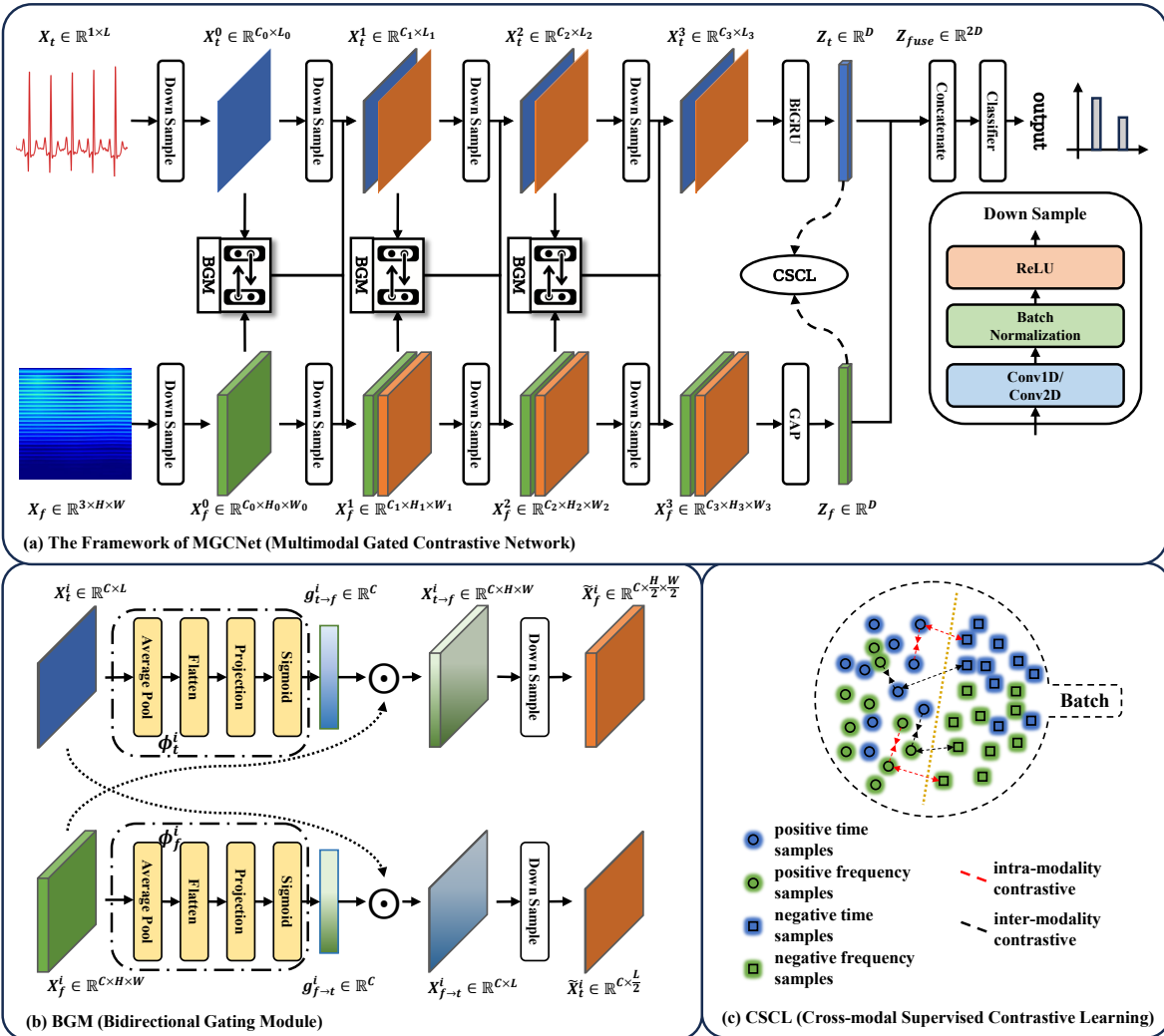


**Figure 2.** (a) The full multimodal network for AF detection; (b) The BGM enabling dynamic interaction between time- and frequency-domain features; (c) The CSCL that enforces discriminative embedding alignment across modalities.

## Methods

### Overall Architecture

Given an input ECG segment  $\mathbf{X}_t \in \mathbb{R}^{1 \times L}$  of length  $L$ , our proposed **MGCNet** processes it through two parallel branches to extract complementary temporal and spectral representations. As illustrated in Figure. 2, the framework comprises the following stages: **Dual-branch Feature Extraction**: The *time-domain branch* takes the raw ECG signal  $\mathbf{X}_t$  and extracts a temporal feature map  $\mathbf{X}_t^i \in \mathbb{R}^{C_i \times L_i}$  using a 1D convolutional neural network (1D-CNN) encoder. The *frequency-domain branch* first converts  $\mathbf{X}_t$  into a frequency representation via the Short-Time Fourier Transform (STFT)<sup>39</sup>, resulting in a spectrogram  $\mathbf{X}_f \in \mathbb{R}^{3 \times H \times W}$ . This spectrogram is then encoded by a 2D-CNN backbone to produce a spectral feature map  $\mathbf{X}_f^i \in \mathbb{R}^{C_i \times H_i \times W_i}$ . Through careful design, both branches output features with the same channel dimension  $C_i$ , facilitating subsequent cross-modal interaction. Here,  $L_i$  denotes the downsampled sequence length in the temporal branch, while  $H_i, W_i$  represent the spatial height and width of the spectral feature map after downsampling.

**Bidirectional Gated Module (BGM)**: To facilitate mutual refinement between modalities, the temporal feature map  $\mathbf{X}_t^i$  and the spectral feature map  $\mathbf{X}_f^i$  are jointly processed by a *Bidirectional Gated Module*, which enables adaptive cross-modal information exchange. The module generates enhanced representations  $\tilde{\mathbf{X}}_t^i$  and  $\tilde{\mathbf{X}}_f^i$  that incorporate complementary cues from the other modality. These refined features are then concatenated with their original counterparts along the channel dimension:

$$\mathbf{X}_t^{i+1} = [\mathbf{X}_t^i; \tilde{\mathbf{X}}_t^i], \mathbf{X}_f^{i+1} = [\mathbf{X}_f^i; \tilde{\mathbf{X}}_f^i], \quad (4)$$

where  $[\cdot; \cdot]$  denotes channel-wise concatenation, and the stage index  $i \in \{0, 1, 2\}$  corresponds to successive downsampling levels in the encoder.

**Modality-specific Global Aggregation**: The augmented temporal feature from the final stage,  $\mathbf{X}_t^3 \in \mathbb{R}^{C_3 \times L_3}$  is first refined by a channel-mixing 1D convolutional layer to enhance inter-channel interactions, then processed by a bidirectional GRU (BiGRU)<sup>40</sup> to capture long-range temporal dynamics. The forward and backward terminal hidden states are concatenated and projected to a  $D$ -dimensional space, yielding the final temporal embedding  $\mathbf{Z}_t \in \mathbb{R}^D$ :

$$\mathbf{Z}_t = \text{BiGRU}(\mathbf{X}_t^3). \quad (5)$$

Similarly, the augmented spectral feature  $\mathbf{X}_f^3 \in \mathbb{R}^{C_3 \times H_3 \times W_3}$  is first refined by a channel-mixing 2D convolutional layer, followed by global average pooling (GAP) over the spatial dimensions to produce the spectral embedding  $\mathbf{Z}_f \in \mathbb{R}^D$ :

$$\mathbf{Z}_f = \frac{1}{H_3 \times W_3} \sum_{m=1}^{H_3} \sum_{n=1}^{W_3} \mathbf{X}_f^3. \quad (6)$$

**Cross-modal Supervised Contrastive Learning (CSCL)**: The temporal embedding  $\mathbf{Z}_t$  and spectral embedding  $\mathbf{Z}_f$  are jointly optimized through a dual-level supervised contrastive loss that operates at both intra-modal and inter-modal levels, guided solely by class labels<sup>41</sup>. The *intra-modal contrastive loss*  $\mathcal{L}_{\text{cont}}^{\text{intra}}$  encourages embeddings of the same class within each modality to cluster tightly while separating those of different classes. The *inter-modal contrastive loss*  $\mathcal{L}_{\text{cont}}^{\text{inter}}$  treats any temporal–spectral embedding pair sharing the same class label as a positive pair and pulls them closer in the joint embedding space; conversely, pairs with mismatched labels are repelled. The total contrastive objective is defined as:

$$\mathcal{L}_{\text{cont}} = \frac{1}{2N} \sum_{i=1}^N \left( \mathcal{L}_{\text{cont}}^{\text{intra}} + \mathcal{L}_{\text{cont}}^{\text{inter}} \right). \quad (7)$$

Here,  $N$  represents the number of samples in the current mini-batch.

**Concatenation and Classification**: The modality-specific embeddings  $\mathbf{Z}_t$  and  $\mathbf{Z}_f$  are fused via a concatenation mechanism:

$$\mathbf{Z}_{\text{fuse}} = [\mathbf{Z}_t; \mathbf{Z}_f]. \quad (8)$$

The fused representation  $\mathbf{Z}_{\text{fuse}}$  is passed through a classifier head to produce logits  $p$ , and the classification loss is:

$$\mathcal{L}_{\text{cls}} = -\frac{1}{N} \sum_{i=1}^N \left[ y^{(i)} \log p^{(i)} + (1 - y^{(i)}) \log(1 - p^{(i)}) \right]. \quad (9)$$

Here,  $N$  represents the number of samples in the current mini-batch.  $y^{(i)} \in \{0, 1\}$  is the true binary label of the  $i$ -th sample;  $p^{(i)} \in (0, 1)$  is the probability that the  $i$ -th sample predicted by the model belongs to the positive class. The final loss function is:

$$\mathcal{L}_{\text{total}} = \mathcal{L}_{\text{cls}} + \lambda \mathcal{L}_{\text{cont}}, \quad (10)$$

where  $\lambda$  is the hyperparameter. The final network structure is shown in Table 2.

**Table 2.** Architecture of the proposed MGCNet.  $B$  denotes batch size,  $N$  denotes number of classifications. All convolutional layers are followed by batch normalization and ReLU activation (not shown for brevity).

Stage	Module	Time Input	Time Output	Freq Input	Freq Output
Initial	Time Init	[ $B, 1, 2500$ ]	[ $B, 32, 1250$ ]	—	—
	Freq Init	—	—	[ $B, 3, 128, 128$ ]	[ $B, 32, 64, 64$ ]
Level 1	BGM-1	[ $B, 32, 1250$ ]	[ $B, 32, 625$ ]	[ $B, 32, 64, 64$ ]	[ $B, 32, 32, 32$ ]
	Downsample-1	[ $B, 32, 1250$ ]	[ $B, 32, 625$ ]	[ $B, 32, 64, 64$ ]	[ $B, 32, 32, 32$ ]
	Concat + Expand-1	[ $B, 64, 625$ ]	[ $B, 64, 625$ ]	[ $B, 64, 32, 32$ ]	[ $B, 64, 32, 32$ ]
Level 2	BGM-2	[ $B, 64, 625$ ]	[ $B, 64, 313$ ]	[ $B, 64, 32, 32$ ]	[ $B, 64, 16, 16$ ]
	Downsample-2	[ $B, 64, 625$ ]	[ $B, 64, 313$ ]	[ $B, 64, 32, 32$ ]	[ $B, 64, 16, 16$ ]
	Concat + Expand-2	[ $B, 128, 313$ ]	[ $B, 128, 313$ ]	[ $B, 128, 16, 16$ ]	[ $B, 128, 16, 16$ ]
Level 3	BGM-3	[ $B, 128, 313$ ]	[ $B, 128, 157$ ]	[ $B, 128, 16, 16$ ]	[ $B, 128, 8, 8$ ]
	Downsample-3	[ $B, 128, 313$ ]	[ $B, 128, 157$ ]	[ $B, 128, 16, 16$ ]	[ $B, 128, 8, 8$ ]
	Concat + Expand-3	[ $B, 256, 157$ ]	[ $B, 256, 157$ ]	[ $B, 256, 8, 8$ ]	[ $B, 256, 8, 8$ ]
Fusion	GRU	[ $B, 256, 157$ ]	[ $B, 256$ ]	—	—
	Global AvgPool	—	—	[ $B, 256, 8, 8$ ]	[ $B, 256$ ]
	Fusion + Classifier	[ $B, 512$ ]	[ $B, N$ ]	—	—

### Bidirectional Gated Module

As shown in Figure 2, the **BGM** enables adaptive cross-modal interaction while progressively reducing spatio-temporal resolution. At hierarchical stage  $i$ , given the temporal feature map  $\mathbf{X}_t^i \in \mathbb{R}^{C_i \times L_i}$  and spectral feature map  $\mathbf{X}_f^i \in \mathbb{R}^{C_i \times H_i \times W_i}$ , BGM generates cross-modal gating signals to selectively enhance informative channels. Specifically, a global context vector is extracted from each modality via adaptive pooling and used to modulate the other.

$$\mathbf{g}_{f \rightarrow t}^i = \phi_f^i(\mathbf{X}_f^i) = \sigma(\mathbf{W}_f^i \cdot \text{GAP}_{2D}(\mathbf{X}_f^i)), \quad (11)$$

$$\mathbf{g}_{t \rightarrow f}^i = \phi_t^i(\mathbf{X}_t^i) = \sigma(\mathbf{W}_t^i \cdot \text{GAP}_{1D}(\mathbf{X}_t^i)), \quad (12)$$

where  $\text{GAP}_{2D}(\cdot)$  and  $\text{GAP}_{1D}(\cdot)$  denote global average pooling over spatial dimensions ( $H, W$ ) and temporal dimension  $L$ , respectively;  $\mathbf{W}_t^i, \mathbf{W}_f^i \in \mathbb{R}^{C_i \times C_i}$  are linear projection matrices; and  $\sigma$  is the sigmoid activation that produces channel-wise gating weights in  $(0, 1)$ . The gating signals are broadcast across their respective spatial or temporal dimensions and applied multiplicatively to modulate the original features:

$$\mathbf{X}_{f \rightarrow t}^i = \mathbf{X}_t^i \otimes \mathbf{g}_{f \rightarrow t}^i, \mathbf{X}_{t \rightarrow f}^i = \mathbf{X}_f^i \otimes \mathbf{g}_{t \rightarrow f}^i, \quad (13)$$

with  $\otimes$  indicating broadcast multiplication. Finally, the gated features are downsampled via strided convolutions to produce outputs for the next stage:

$$\tilde{\mathbf{X}}_t^i = \text{Conv1D}(\mathbf{X}_{f \rightarrow t}^i), \tilde{\mathbf{X}}_f^i = \text{Conv2D}(\mathbf{X}_{t \rightarrow f}^i). \quad (14)$$

### Cross-modal Supervised Contrastive Learning

In order to implement the **CSCL** module, we employ a dual-level supervised contrastive loss to enforce both intra-modal discrimination and inter-modal alignment. Let  $\mathbf{Z}_t^{(i)}, \mathbf{Z}_f^{(i)}$  be L2-normalized embeddings of sample  $i$  with label  $y^{(i)} \in \{0, 1\}$ , and  $\text{sim}(\mathbf{u}, \mathbf{v}) = \frac{\mathbf{u}^\top \mathbf{v}}{\|\mathbf{u}\| \|\mathbf{v}\|}$  denote cosine similarity. The **intra-modal loss** pulls together same-class samples within each modality:

$$\mathcal{L}_{\text{cont}}^{\text{intra}} = -\log \frac{\sum_{j \neq i, y^{(j)}=y^{(i)}} \exp(\text{sim}(\mathbf{z}_t^{(i)}, \mathbf{z}_t^{(j)}) / \tau)}{\sum_{k \neq i} \exp(\text{sim}(\mathbf{z}_t^{(i)}, \mathbf{z}_t^{(k)}) / \tau)} + (t \leftrightarrow f). \quad (15)$$

The **inter-modal loss** aligns cross-modal representations of the same class:

$$\mathcal{L}_{\text{cont}}^{\text{inter}} = -\log \frac{\sum_{j, y^{(j)}=y^{(i)}} \exp(\text{sim}(\mathbf{z}_t^{(i)}, \mathbf{z}_f^{(j)}) / \tau)}{\sum_{k=1}^N \exp(\text{sim}(\mathbf{z}_t^{(i)}, \mathbf{z}_f^{(k)}) / \tau)} + (t \leftrightarrow f), \quad (16)$$

where  $(t \leftrightarrow f)$  denotes the symmetric term for spectral embeddings, temperature  $\tau > 0$ .

## Results

### Evaluation Metrics

To comprehensively evaluate the performance of our method on AF detection, we report six standard evaluation metrics: *Accuracy*, *Area Under the ROC Curve (AUC)*, *Precision*, *Recall (Sensitivity)*, *F1-score*, and *Specificity*. Let TP, TN, FP, and FN denote the numbers of true positives, true negatives, false positives, and false negatives, respectively. The metrics are defined as follows:

- **Accuracy** measures the overall fraction of correctly classified samples:  $\text{Accuracy} = \frac{\text{TP} + \text{TN}}{\text{TP} + \text{TN} + \text{FP} + \text{FN}}$
- **Precision** (Positive Predictive Value) is the proportion of samples predicted as positive that are truly positive:  $\text{Precision} = \frac{\text{TP}}{\text{TP} + \text{FP}}$
- **Recall** (Sensitivity or True Positive Rate) is the proportion of actual positive samples that are correctly identified:  $\text{Recall} = \frac{\text{TP}}{\text{TP} + \text{FN}}$
- **Specificity** (True Negative Rate) is the proportion of actual negative samples that are correctly identified:  $\text{Specificity} = \frac{\text{TN}}{\text{TN} + \text{FP}}$
- **F1-score** is the harmonic mean of Precision and Recall, providing a balanced measure of the two:  $\text{F1} = 2 \cdot \frac{\text{Precision} \cdot \text{Recall}}{\text{Precision} + \text{Recall}}$
- **AUC** (Area Under the ROC Curve) quantifies the model's ability to discriminate between positive and negative classes across all decision thresholds. It is computed as the area under the curve of True Positive Rate (TPR = Recall) versus False Positive Rate (FPR = 1 – Specificity). An AUC value closer to 1.0 indicates better discriminative performance.

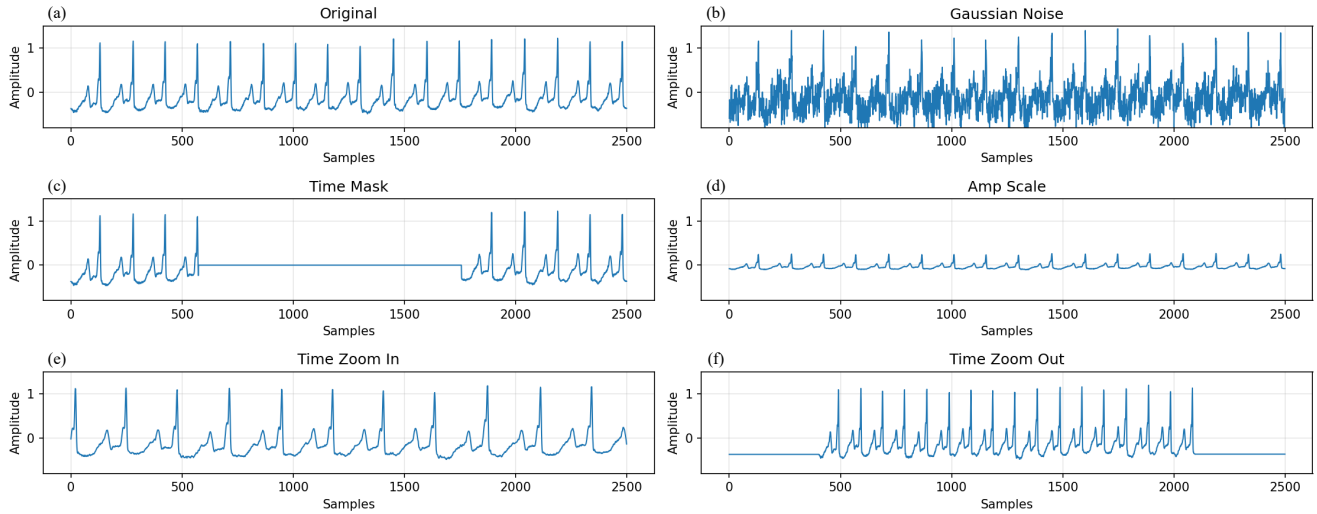


**Figure 3.** Illustration of the ECG data augmentation strategies applied in our experiments. (a) Original 10-second ECG segment; (b) with added Gaussian noise; (c) with random time masking; (d) with amplitude scaling; (e) with time zoom in; (f) with time zoom out.

### Implementation Details

All experiments were implemented in PyTorch 2.4.1 with CUDA 11.5 acceleration and conducted on a workstation equipped with an NVIDIA GeForce RTX 3090 GPU (24 GB VRAM) and an Intel Core i7-12700KF CPU. To enhance all model robustness against real-world signal variability, we applied four data augmentation strategies to the training set (see Figure. 3 for visual examples): (i) additive Gaussian noise with standard deviation  $\sigma \in [0, 0.2]$ ; (ii) random masking with a masking ratio uniformly sampled from  $[0, 0.1]$ ; (iii) amplitude scaling by a factor drawn from  $\mathcal{U}(0.5, 1.5)$ ; and (iv) time-axis zooming (stretching or compression) with scale factors in  $[0.8, 1.2]$ , implemented via linear interpolation.

The model was trained for 25 epochs with a batch size of 128. We used the Adam optimizer<sup>42</sup> with an initial learning rate of  $1 \times 10^{-3}$ , weight decay of  $1 \times 10^{-4}$ , and an inverse-time learning rate scheduler defined as:  $\eta_t = \eta_0 / (1 + \gamma \cdot t)$ , where  $\eta_0 = 10^{-3}$ , decay rate  $\gamma = 10^{-4}$ , and  $t$  denotes the epoch index. The contrastive loss hyperparameters were configured as  $\lambda = 0.01$  and  $\tau = 0.1$ .

Critically, we adopted a patient-wise five-fold cross-validation protocol: all segments derived from the same patient were assigned exclusively to one fold. This strategy eliminates inter-patient data leakage and ensures that performance metrics reflect robustness to unseen individuals. Furthermore, patient assignment was stratified to maintain balanced atrial fibrillation (AF) and normal sinus rhythm (N) proportions across all folds.

To further assess the model's generalization to domain shift, we performed bidirectional cross-dataset evaluation. Specifically, we trained the model on one dataset and directly evaluated it on another without any fine-tuning or adaptation. Two scenarios were considered: (i) training on the AFDB and testing on CPSC2021; and (ii) training on CPSC2021 and testing on AFDB.

**Table 3.** Performance comparison of different models on AFDB and CPSC2021. The best results in each setting are highlighted in bold.

Model	Evaluation Metrics   Mean (standard deviation)					
	Acc	AUC	F1	Precision	Recall	Specificity
<b>Dataset: AFDB</b>						
SCCNN(2023) <sup>23</sup>	0.9614 (0.0198)	0.9907 (0.0050)	0.9481 (0.0279)	0.9473 (0.0285)	0.9502 (0.0427)	0.9681 (0.0172)
IMCResNet(2024) <sup>20</sup>	0.9514 (0.0362)	0.9836 (0.0175)	0.9356 (0.0472)	0.9412 (0.0503)	0.9318 (0.0581)	0.9631 (0.0350)
MoETransformer(2024) <sup>18</sup>	0.9453 (0.0309)	0.9857 (0.0096)	0.9259 (0.0431)	0.9363 (0.0450)	0.9170 (0.0543)	0.9622 (0.0265)
SeqAFNet(2024) <sup>19</sup>	0.9374 (0.0341)	0.9822 (0.0127)	0.9170 (0.0462)	0.9197 (0.0619)	0.9212 (0.0780)	0.9473 (0.0450)
MFEGNet(2025) <sup>22</sup>	0.9794 (0.0132)	0.9957 (0.0045)	0.9730 (0.0169)	0.9697 (0.0247)	0.9767 (0.0209)	0.9809 (0.0156)
MSCGN(2026) <sup>21</sup>	0.9812 (0.0155)	0.9965 (0.0042)	0.9755 (0.0193)	0.9771 (0.0311)	0.9774 (0.0164)	0.9832 (0.0209)
<b>MGCNet (Ours)</b>	<b>0.9878</b> <b>(0.0094)</b>	<b>0.9987</b> <b>(0.0013)</b>	<b>0.9841</b> <b>(0.0120)</b>	<b>0.9856</b> <b>(0.0219)</b>	<b>0.9830</b> <b>(0.0170)</b>	<b>0.9906</b> <b>(0.0147)</b>
<b>Dataset: CPSC2021</b>						
SCCNN(2023) <sup>23</sup>	0.9713 (0.0087)	0.9900 (0.0136)	0.9588 (0.0119)	0.9576 (0.0239)	0.9605 (0.0136)	0.9767 (0.0148)
IMCResNet(2024) <sup>20</sup>	0.9337 (0.0204)	0.9819 (0.0113)	0.9253 (0.0299)	0.9024 (0.0444)	0.9096 (0.0273)	0.9459 (0.0293)
MoETransformer(2024) <sup>18</sup>	0.9524 (0.0183)	0.9908 (0.0062)	0.9307 (0.0291)	0.9287 (0.0268)	0.9338 (0.0435)	0.9622 (0.0139)
SeqAFNet(2024) <sup>19</sup>	0.9539 (0.0181)	0.9914 (0.0064)	0.9341 (0.0239)	0.9352 (0.0524)	0.9369 (0.0418)	0.9623 (0.0361)
MFEGNet(2025) <sup>22</sup>	0.9797 (0.0177)	0.9972 (0.0042)	<b>0.9719</b> <b>(0.0226)</b>	0.9610 (0.0460)	<b>0.9846</b> <b>(0.0113)</b>	0.9767 (0.0297)
MSCGN(2026) <sup>21</sup>	0.9776 (0.0140)	0.9973 (0.0032)	0.9684 (0.0184)	0.9611 (0.0357)	0.9766 (0.0072)	0.9778 (0.0222)
<b>MGCNet (Ours)</b>	<b>0.9801</b> <b>(0.0042)</b>	<b>0.9979</b> <b>(0.0010)</b>	0.9715 (0.0067)	<b>0.9639</b> <b>(0.0058)</b>	0.9794 (0.0124)	<b>0.9806</b> <b>(0.0023)</b>

## Comparative Experiments

To validate the effectiveness of the proposed **MGCNet**, we conducted comprehensive experiments on two widely used ECG datasets: AFDB and CPSC2021. Following standard practice, we performed patient-wise five-fold cross-validation to prevent data leakage across subjects. For a fair comparison, all competing methods were trained and evaluated under identical experimental settings, including the same data preprocessing pipeline and data augmentation strategies. We compared our method against six representative baseline approaches:

- (1) **SCCNN**<sup>23</sup>, which reshapes 1D ECG signals into a 2D "Z-shaped" representation and processes them with a 2D CNN;
- (2) **IMCResNet**<sup>20</sup>, a multi-scale convolutional architecture that captures interactions across different receptive fields;
- (3) **MoETransformer**<sup>18</sup>, which integrates Mixture-of-Experts (MoE) modules into a standard Transformer to enhance representational diversity;

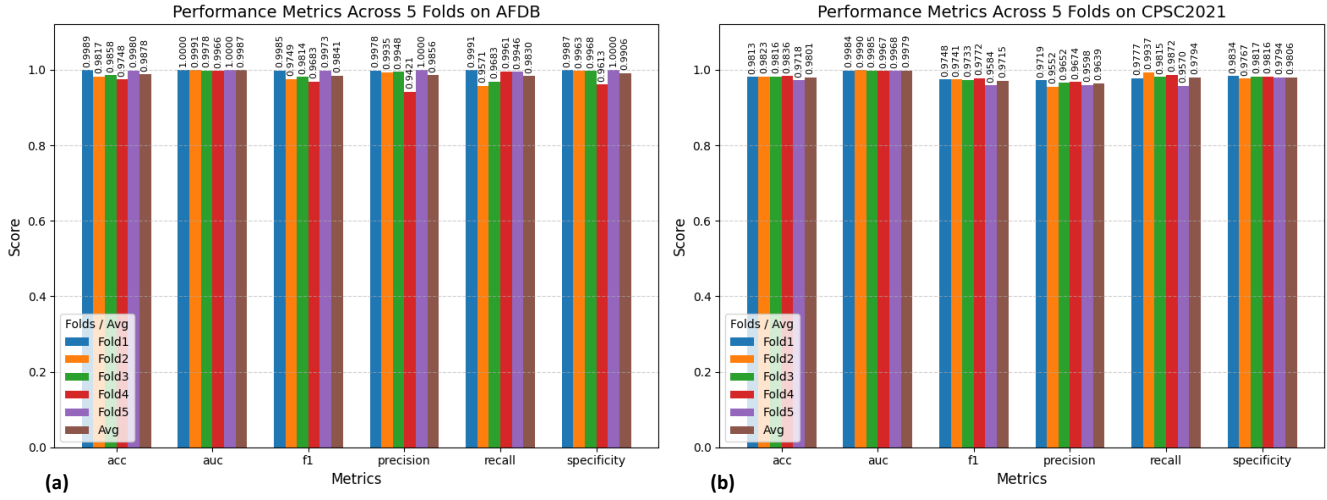


**Figure 4.** Five-fold cross-validation results on two datasets across six metrics (Accuracy, AUC, F1-score, Precision, Recall and Specificity).

- (4) **SeqAFNet**<sup>19</sup>, a dual-path RNN framework designed to jointly model local and global temporal dependencies;
- (5) **MFEGLNet**<sup>22</sup>, which employs multi-scale gated attention mechanisms for adaptive feature refinement;
- and (6) **MSCGN**<sup>21</sup>, a network incorporating complementary multi-scale contextual modules.

As shown in Table 3, our method achieved the best performance on four out of six evaluation metrics on both AFDB and CPSC2021, demonstrating its consistent superiority across diverse assessment criteria. Notably, MGCNet attained the highest accuracy of **0.9878** on AFDB and **0.9801** on CPSC2021 among all compared methods, highlighting its strong robustness in real-world arrhythmia detection scenarios.

To evaluate the stability and reliability of MGCNet, we visualized its five-fold cross-validation results on the AFDB and CPSC2021 datasets (see Figure. 4). The bar plots showed the average performance across the five folds for six evaluation metrics: Accuracy, AUC, F1-score, Precision, Recall, and Specificity. As confirmed by the standard deviation values reported in Table. 3, the variability across all metrics and both datasets remained around 0.02, demonstrating that our method exhibits strong robustness and reproducibility under different patient-wise data partitions.

## Generalization Experiments

To evaluate the generalization of the proposed framework to distributional discrepancies commonly encountered in real-world clinical settings, we conducted cross-dataset experiments between the AFDB and the CPSC2021. These two datasets differ markedly in sampling rates (250 Hz vs. 200 Hz), signal duration and so on—posing a significant challenge for model generalization.

As shown in Table 4, MGCNet consistently outperformed all compared methods across both transfer directions and most evaluation metrics. When trained on AFDB and tested on CPSC2021, our method achieved an accuracy of 0.9165 and an AUC of 0.9643, surpassing the previous best result (MSCGN, 0.8951 accuracy) by over 2.1 percentage points. More notably, in the reverse setting—training on CPSC2021 and testing on AFDB—MGCNet attained 0.9507 accuracy and an exceptional AUC of 0.9894, with specificity reaching 0.9719, indicating a strong capability to suppress false positives, a critical requirement for AF screening in low-prevalence populations.

While MGCNet exhibited slightly lower recall (by approximately 3–5 percentage points) compared to certain baselines under domain shift, this trade-off aligns with clinical priorities in real-world deployment: minimizing false alarms is often more crucial than capturing every possible case, especially in resource-constrained or wearable-based monitoring scenarios where excessive false positives can lead to alert fatigue, unnecessary referrals, and reduced user trust. The BGM and CSCL modules appear to prioritize the extraction of high-confidence, domain-invariant features, favoring specificity over maximal sensitivity, which enhances reliability in heterogeneous clinical environments.

The performance gap between MGCNet and existing approaches was particularly pronounced in precision and specificity under domain shift, suggesting that the BGM and CSCL effectively promote the extraction of domain-invariant, physiologically meaningful features. Overall, these results confirm that the proposed architecture not only excels in intra-dataset scenarios but also demonstrates superior adaptability and clinically appropriate robustness across diverse data sources—a key prerequisite for

multi-center or community-based AF screening systems.

**Table 4.** Cross-dataset generalization performance of MGCNet and competing methods. Training on AFDB and testing on CPSC2021 (top), and vice versa (bottom). The best results in each setting are highlighted in bold.

Model	Evaluation Metrics					
	Acc	AUC	F1	Precision	Recall	Specificity
<b>AFDB → CPSC2021</b>						
SCCNN(2023) <sup>23</sup>	0.8386	0.9497	0.8021	0.6969	0.9448	0.7823
IMCResNet(2024) <sup>20</sup>	0.8504	0.9319	0.7982	0.7489	0.8545	0.8482
MoETransformer(2024) <sup>18</sup>	0.8681	0.9355	0.8165	0.7878	0.8474	0.8971
SeqAFNet(2024) <sup>19</sup>	0.8646	0.9382	0.8165	0.7691	0.8701	0.8617
MFEGNet(2025) <sup>22</sup>	0.8843	0.9593	0.8515	0.7663	<b>0.9579</b>	0.8453
MSCGN(2026) <sup>21</sup>	0.8951	0.9609	0.8611	0.7947	0.9397	0.8714
<b>MGCNet(Ours)</b>	<b>0.9165</b>	<b>0.9643</b>	<b>0.8819</b>	<b>0.8639</b>	0.9007	<b>0.9248</b>
<b>CPSC2021 → AFDB</b>						
SCCNN(2023) <sup>23</sup>	0.8413	0.9140	0.7907	0.7828	0.7987	0.8669
IMCResNet(2024) <sup>20</sup>	0.7706	0.8240	0.7274	0.6564	0.8157	0.7435
MoETransformer(2024) <sup>18</sup>	0.7490	0.8535	0.6840	0.6483	0.7238	0.7642
SeqAFNet(2024) <sup>19</sup>	0.8297	0.9272	0.7870	0.6940	0.9088	0.7878
MFEGNet(2025) <sup>22</sup>	0.8756	0.9620	0.8450	0.7935	0.9037	0.8588
MSCGN(2026) <sup>21</sup>	0.9164	0.9504	0.8947	0.8483	<b>0.9465</b>	0.8983
<b>MGCNet(Ours)</b>	<b>0.9507</b>	<b>0.9894</b>	<b>0.9331</b>	<b>0.9514</b>	0.9154	<b>0.9719</b>

### Ablation Experiments

We further conducted an ablation study to evaluate the impact of key components, namely the BGM and CSCL, on both intra-dataset performance and cross-dataset generalization. All variants were trained under identical protocols.

As shown in Table 5, the full MGCNet consistently achieved the highest accuracy and AUC across all settings. Removing BGM led to noticeable performance degradation, particularly under domain shift, where both accuracy and AUC dropped substantially compared to the full model. This highlighted BGM’s role in aligning time-frequency representations across heterogeneous data distributions. Similarly, ablating CSCL resulted in reduced discriminability, with pronounced declines observed in cross-dataset scenarios than in intra-dataset evaluation. This suggested that CSCL not only improves feature quality within a dataset but also enhances robustness to distributional shifts by promoting consistent hierarchical representations.

Single-branch variants (time-only or frequency-only) performed significantly worse, especially in cross-dataset tests, confirming that multimodal fusion is essential for reliable AF detection across diverse clinical recording conditions.

Overall, both BGM and CSCL contributed critically to strong robustness and generalization, as evidenced by consistent gains in both accuracy and AUC, which demonstrating their value for real-world ECG monitoring applications.

**Table 5.** Ablation study of key components in MGCNet under intra-dataset and cross-dataset settings. Results are reported as accuracy / AUC.

Model Variant	Intra-Dataset		Cross-Dataset	
	AFDB	CPSC2021	AFDB → CPSC2021	CPSC2021 → AFDB
Full MGCNet (Ours)	<b>0.9878 / 0.9987</b>	<b>0.9801 / 0.9979</b>	<b>0.9165 / 0.9643</b>	<b>0.9507 / 0.9894</b>
w/o BGM	0.9732 / 0.9961	0.9645 / 0.9952	0.8721 / 0.9487	0.8934 / 0.9621
w/o CSCL	0.9785 / 0.9970	0.9710 / 0.9963	0.8893 / 0.9532	0.9102 / 0.9745
Time-only	0.9621 / 0.9934	0.9533 / 0.9921	0.8247 / 0.9215	0.8416 / 0.9302
Freq-only	0.9587 / 0.9928	0.9496 / 0.9915	0.8089 / 0.9103	0.8273 / 0.9187

### Sensitivity Analysis

We further analyzed the impact of the supervised contrastive loss weight  $\lambda_{\text{cont}}$  on model performance, while keeping the cross-entropy weight fixed at 1. The ablation included  $\lambda_{\text{cont}} \in \{0, 0.001, 0.01, 0.1, 1.0\}$ , where  $\lambda_{\text{cont}} = 0$  corresponds to training with cross-entropy alone.

As shown in Figure 5, both accuracy and AUC improved when a small contrastive term was introduced ( $\lambda_{\text{cont}} = 0.001$ ), compared to the cross-entropy-only baseline. Performance peaked at  $\lambda_{\text{cont}} = 0.01$ , achieving an accuracy of 0.9801 and AUC of 0.9979 on CPSC2021, and 0.9507 / 0.9894 under cross-dataset evaluation. Further increasing  $\lambda_{\text{cont}}$  led to slight degradation, indicating that excessive emphasis on representation learning can interfere with the primary diagnostic objective.

These results demonstrated that a modest contribution from supervised contrastive learning, specifically  $\lambda_{\text{cont}} = 0.01$ , effectively regularized the model and enhanced robustness and generalization, without compromising classification fidelity.

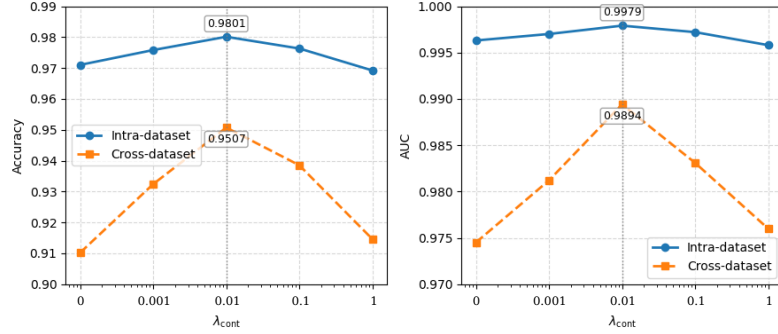


**Figure 5.** Accuracy and AUC versus  $\lambda_{\text{cont}}$  on CPSC2021 (intra) and CPSC2021  $\rightarrow$  AFDB (cross).

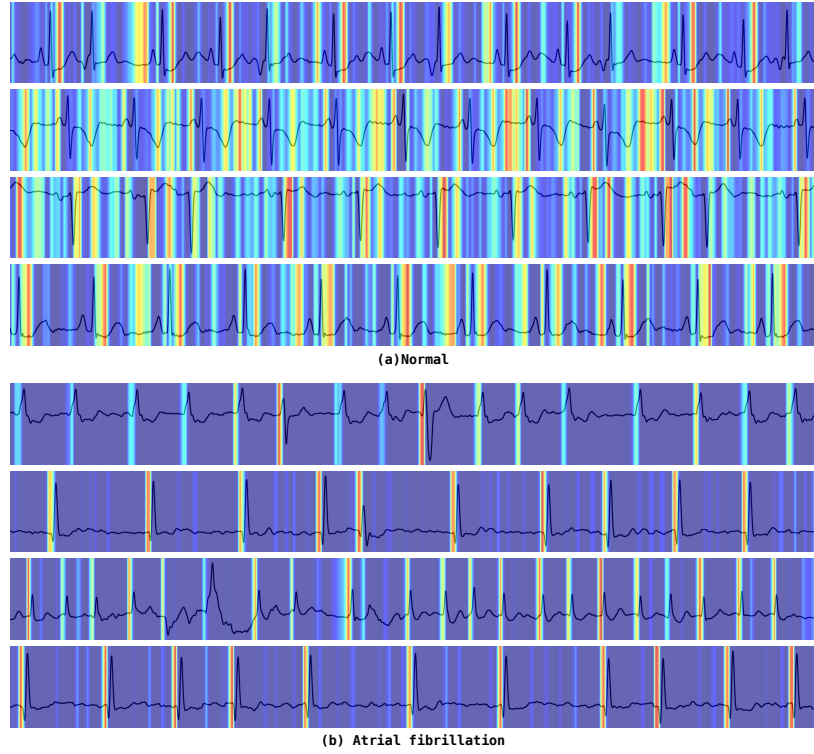


**Figure 6.** Grad-CAM attention maps overlaid on ECG waveforms. Redder regions indicate higher model attention, while bluer regions indicate lower attention. Top: Normal sinus rhythm shows diffuse activation across the cardiac cycle. Bottom: Atrial fibrillation exhibits concentrated attention near the P-wave region, where organized atrial activity is lost.

## Interpretability

We employed Gradient-weighted Class Activation Mapping (Grad-CAM)<sup>43</sup> on the time-domain ECG to examine which segments most influenced the model's predictions as shown in Figure 6. For AF samples, Grad-CAM consistently highlighted

the P-wave region—where organized atrial activity normally occurs but is typically absent or irregular in AF. This suggested the model learned to detect the loss of regular atrial depolarization, consistent with clinical AF criteria.

In normal samples, activation was more dispersed across the P-wave, QRS complex, and T-wave, with no dominant focal region. This reflected the absence of pathological markers; the model likely relied on global waveform morphology and rhythm regularity rather than a single diagnostic feature.

Grad-CAM maps were upsampled via linear interpolation from lower-resolution feature maps to match the input signal length. While this may cause mild smoothing or minor positional shifts, the regional activation trends remained robust and clinically plausible.

**Table 6.** Comparison of computational complexity (FLOPs) and model size (parameters) across ECG AF detection models.

Model	FLOPs (G)	Params (M)
SCCNN (2023) <sup>23</sup>	2.07	2.03
IMCResNet (2024) <sup>20</sup>	2.09	0.84
MoETransformer (2024) <sup>18</sup>	1.12	2.05
SeqAFNet (2024) <sup>19</sup>	1.04	2.82
MFEGNet (2025) <sup>22</sup>	1.12	4.71
MSCGN (2026) <sup>21</sup>	0.50	1.38
<b>MGCNet (Ours)</b>	<b>0.96</b>	<b>1.96</b>

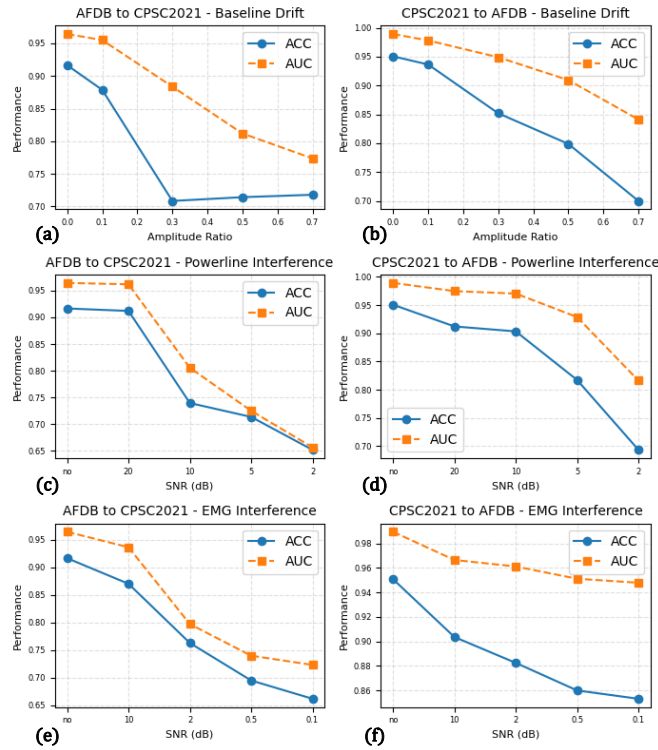


**Figure 7.** Robustness of cross-dataset AF classification under increasing levels of ECG interference. Left column: performance of AFDB → CPSC2021 transfer; right column: CPSC2021 → AFDB. From top to bottom: (a,b) baseline drift(0.1 Hz, amplitude ratio 0–0.7), (c,d) powerline interference (50 Hz fundamental with two harmonics, SNR =  $\infty$ /no to 2 dB), and (e,f) EMG interference (band-limited to 20–500 Hz, SNR =  $\infty$ /no to 0.1 dB). Solid lines with circles denote accuracy (ACC); dashed lines with squares denote AUC.

## Discussion

### Efficiency

Computational efficiency is essential for deploying ECG analysis models in resource-constrained clinical or edge environments. As shown in Table 6, our MGCNet achieves a favorable trade-off between model size and computational cost, requiring only 0.96 G FLOPs and 1.96 M parameters—lower than most recent AF detection models such as SCCNN, IMCResNet, SeqAFNet, and MFEGNet. While MSCGN reports the lowest FLOPs (0.50 G), its smaller capacity may compromise representation ability, especially for noisy or heterogeneous ECGs. In contrast, MGCNet maintains sufficient expressiveness to effectively fuse time- and frequency-domain features without excessive overhead.

Combined with supervised contrastive learning, which improves feature quality without adding inference cost, our approach demonstrates that strong robustness and generalizability can be achieved alongside high efficiency, making it suitable for deployment on portable or embedded cardiac monitoring devices<sup>4445</sup>.

### Anti-interference

To address three common sources of degradation in real-world ECG recordings—baseline drift, powerline interference, and electromyographic (EMG) interference<sup>4647</sup>—we systematically evaluated the model’s anti-interference capability under two cross-dataset transfer settings: AFDB → CPSC2021 and CPSC2021 → AFDB. The result is shown in the Figure. 7.

Baseline drift was simulated as a low-frequency sinusoidal modulation (0.1 Hz) with increasing amplitude ratios. Performance deteriorated significantly once the distortion exceeded a moderate level, particularly in the AFDB → CPSC2021 direction, indicating that excessive low-frequency drift can obscure critical morphological cues essential for accurate classification.

Powerline interference was introduced as a composite signal comprising a 50 Hz fundamental and its first two harmonics, with signal-to-noise ratio (SNR) progressively reduced. The model exhibited robustness at mild interference levels but experienced pronounced performance loss under severe contamination.

EMG interference was synthesized as band-limited Gaussian noise (20–500 Hz) across a wide SNR range. In this setting, performance declined more gradually compared to powerline interference, and the CPSC2021 → AFDB direction maintained substantially higher robustness even under extreme noise conditions.

Collectively, these findings highlight that while the model remains vulnerable to intense low-frequency and narrowband interference, it achieves meaningful anti-interference performance, thereby supporting its applicability in practical, noise-prone cardiac monitoring environments. Notably, the CPSC2021 → AFDB transfer was consistently more robust, indicating that training on a larger and more diverse dataset improves resilience to interference.

## Conclusions

We presented a robust and generalizable deep learning framework for atrial fibrillation (AF) detection from single-lead ECG signals, combining time- and frequency-domain features through a dedicated fusion architecture. By incorporating supervised contrastive learning, the model learns discriminative embeddings that enhance intra-class compactness and inter-class separation, significantly improving cross-dataset generalization. Experiments across multiple public datasets demonstrate that our approach achieves high accuracy while maintaining strong performance under domain shifts. Post-hoc Grad-CAM analysis further confirms that the model focuses on clinically relevant regions, particularly the P-wave interval in AF cases, where organized atrial activity is typically lost. These results indicate that integrating multi-domain representation with contrastive representation learning is an effective strategy for building reliable, interpretable, and deployable ECG classification systems. Future work will extend this framework to multi-class arrhythmia detection and resource-constrained clinical environments.

## Acknowledgements

During the preparation of this manuscript, the author(s) used Qwen (Alibaba Cloud, Qwen-Max, 2025) for the purposes of language polishing, improving the clarity and flow of the text, and assisting in the drafting of methodological descriptions. The authors have reviewed and edited all AI-generated content and take full responsibility for the accuracy and integrity of the final manuscript.

## Author contributions statement

Conceptualization, H.L., J.W. and X.O.; methodology, H.L., Y.L. and X.O.; software, X.O.; validation, Y.L. and X.O.; formal analysis, H.L., J.W., J.X., M.L., S.L., and X.O.; investigation, X.O.; resources, H.L. and J.X.; data curation, X.O.; writing—original draft preparation, X.O.; writing—review and editing, H.L., Y.L. and J.W.; visualization, X.O.; supervision, H.L. and Y.L.; project administration, H.L., J.X., Y.L. and X.O.; funding acquisition, H.L. All authors have read and agreed to the published version of the manuscript.

## Competing interests

The authors declare no conflicts of interest.

## Data availability

The AFDB dataset is publicly available from PhysioNet (<https://www.physionet.org/content/afdb/1.0.0/>). The CPSC2021 dataset was provided by the China Physiological Signal Challenge 2021 and is accessible via the official challenge website (<https://physionet.org/content/cpsc2021/1.0.0/>). All code and trained models have been made publicly available on GitHub upon publication to ensure reproducibility (<https://github.com/Ou-Young-1999/MGCNet>).

## Informed consent

Not applicable.

## Funding

This research received no external funding.

## References

1. Li, X. *et al.* Global burden and health inequality of atrial fibrillation/atrial flutter from 1990 to 2021. *Front. Cardiovasc. Medicine* **12**, 1585980, DOI: <https://doi.org/10.3389/fcvm.2025.1585980> (2025).
2. Bordignon, S., Corti, M. C. & Bilato, C. Atrial fibrillation associated with heart failure, stroke and mortality. *J. Atr. Fibrillation* **5**, 467, DOI: <https://doi.org/10.4022/jafib.467> (2012).
3. Pamporos, K. *et al.* Prevalence of asymptomatic atrial fibrillation and risk factors associated with asymptomatic status: a systematic review and meta-analysis. *Eur. J. Prev. Cardiol.* zwaf138, DOI: <https://doi.org/10.1093/eurjpc/zwaf138> (2025).
4. Yang, T. Y., Huang, L., Malwade, S., Hsu, C.-Y. & Chen, Y. C. Diagnostic accuracy of ambulatory devices in detecting atrial fibrillation: systematic review and meta-analysis. *JMIR mHealth uHealth* **9**, e26167, DOI: <https://doi.org/10.2196/26167> (2021).
5. Lip, G. Y. & Hee, F. L. S. Paroxysmal atrial fibrillation. *Qjm* **94**, 665–678, DOI: <https://doi.org/10.1093/qjmed/94.12.665> (2001).
6. Stahrenberg, R. *et al.* Enhanced detection of paroxysmal atrial fibrillation by early and prolonged continuous holter monitoring in patients with cerebral ischemia presenting in sinus rhythm. *Stroke* **41**, 2884–2888, DOI: <https://doi.org/10.1161/STROKEAHA.110.591958> (2010).
7. Rahman, M. M. *et al.* Residual-attention deep learning model for atrial fibrillation detection from holter recordings. *J. Electrocardiol.* **89**, 153876, DOI: <https://doi.org/10.1016/j.jelectrocard.2025.153876> (2025).
8. Lin, H. Artificial intelligence with great potential in medical informatics: a brief review. *Medinformatics* **1**, 2–9, DOI: <https://doi.org/10.47852/bonviewMEDIN42022204> (2024).
9. Murat, F. *et al.* Review of deep learning-based atrial fibrillation detection studies. *Int. journal environmental research public health* **18**, 11302, DOI: <https://doi.org/10.3390/ijerph182111302> (2021).
10. Jabbar, A., Huang, J., Jabbar, M. K. & Ali, A. Adaptive multimodal fusion in vertical federated learning for decentralized glaucoma screening. *Brain Sci.* **15**, 990, DOI: <https://doi.org/10.3390/brainsci15090990> (2025).
11. Stahlschmidt, S. R., Ulfenborg, B. & Synnergren, J. Multimodal deep learning for biomedical data fusion: a review. *Briefings bioinformatics* **23**, bbab569, DOI: <https://doi.org/10.1093/bib/bbab569> (2022).
12. Murat, F. *et al.* Review of deep learning-based atrial fibrillation detection studies. *Int. journal environmental research public health* **18**, 11302, DOI: <https://doi.org/10.3390/ijerph182111302> (2021).
13. Mahajan, R., Kamaleswaran, R. & Akbilgic, O. Comparative analysis between convolutional neural network learned and engineered features: A case study on cardiac arrhythmia detection. *Cardiovasc. Digit. Heal. J.* **1**, 37–44, DOI: <https://doi.org/10.1016/j.cvdhj.2020.04.001> (2020).
14. Rao, S. S. & Martis, R. J. Rr interval-based atrial fibrillation detection using traditional and ensemble machine learning algorithms. *J. Med. Signals & Sensors* **13**, 224–232, DOI: [https://doi.org/10.4103/jmss.jmss\\_4\\_22](https://doi.org/10.4103/jmss.jmss_4_22) (2023).

15. Xia, Y., Wulan, N., Wang, K. & Zhang, H. Detecting atrial fibrillation by deep convolutional neural networks. *Comput. biology medicine* **93**, 84–92, DOI: <https://doi.org/10.1016/j.combiomed.2017.12.007> (2018).
16. Faust, O. *et al.* Automated detection of atrial fibrillation using long short-term memory network with rr interval signals. *Comput. biology medicine* **102**, 327–335, DOI: <https://doi.org/10.1016/j.combiomed.2018.07.001> (2018).
17. Laghari, A. A. *et al.* Deep residual-dense network based on bidirectional recurrent neural network for atrial fibrillation detection. *Sci. reports* **13**, 15109, DOI: <https://doi.org/10.1038/s41598-023-40343-x> (2023).
18. Kim, S., Lim, J. & Jang, J. Patient-adaptive beat-wise temporal transformer for atrial fibrillation classification in continuous long-term cardiac monitoring. *IEEE Access* DOI: <https://doi.org/10.1109/ACCESS.2024.3498043> (2024).
19. Kim, S., Lim, J. & Jang, J. Seqafnet: A beat-wise sequential neural network for atrial fibrillation classification in adhesive patch-type electrocardiographs. *IEEE J. Biomed. Heal. Informatics* **28**, 5260–5269, DOI: <https://doi.org/10.1109/JBHI.2024.3411056> (2024).
20. Sun, Y. *et al.* Imc-resnet: Atrial fibrillation detection method based on interlayer multiscale coupling. *Biomed. Signal Process. Control.* **97**, 106683, DOI: <https://doi.org/10.1016/j.bspc.2024.106683> (2024).
21. Wu, X., Yan, M., Tang, H., Wu, D. & Xie, L. Mscgn: Multiscale complementary gating network for time series classification. *Biomed. Signal Process. Control.* **112**, 108563, DOI: <https://doi.org/10.1016/j.bspc.2025.108563> (2026).
22. Wu, X., Yan, M., Wang, R. & Xie, L. Multiscale feature enhanced gating network for atrial fibrillation detection. *Comput. Methods Programs Biomed.* **261**, 108606, DOI: <https://doi.org/10.1016/j.cmpb.2025.108606> (2025).
23. Li, Y. *et al.* Diagnosis of atrial fibrillation using self-complementary attentional convolutional neural network. *Comput. Methods Programs Biomed.* **238**, 107565, DOI: <https://doi.org/10.1016/j.cmpb.2023.107565> (2023).
24. He, R. *et al.* Automatic detection of atrial fibrillation based on continuous wavelet transform and 2d convolutional neural networks. *Front. physiology* **9**, 1206, DOI: <https://doi.org/10.3389/fphys.2018.01206> (2018).
25. Luo, Y., Huang, B., Zhu, J., Zeng, X. & Zhang, Q. Detection of atrial fibrillation with a hybrid deep learning model and time-frequency representations. *medRxiv* 2025–06, DOI: <https://doi.org/10.1101/2025.06.03.25328929> (2025).
26. Yue, Y., Chen, C., Liu, P., Xing, Y. & Zhou, X. Automatic detection of short-term atrial fibrillation segments based on frequency slice wavelet transform and machine learning techniques. *Sensors* **21**, 5302, DOI: <https://doi.org/10.3390/s21165302> (2021).
27. Zhu, H., Jiang, N., Xia, S. & Tong, J. Atrial fibrillation prediction based on recurrence plot and resnet. *Sensors* **24**, 4978, DOI: <https://doi.org/10.3390/s24154978> (2024).
28. He, K., Zhang, X., Ren, S. & Sun, J. Deep residual learning for image recognition. In *Proceedings of the IEEE conference on computer vision and pattern recognition*, 770–778, DOI: <https://doi.org/10.1109/CVPR.2016.90> (2016).
29. Xie, J., Stavrakis, S. & Yao, B. Automated identification of atrial fibrillation from single-lead ecgs using multi-branching resnet. *Front. Physiol.* **15**, 1362185, DOI: <https://doi.org/10.3389/fphys.2024.1362185> (2024).
30. Hu, Y. *et al.* An effective frequency-domain feature of atrial fibrillation based on time–frequency analysis. *BMC Med. informatics decision making* **20**, 308, DOI: <https://doi.org/10.1186/s12911-020-01337-1> (2020).
31. Ma, K., Zhang, T., Zhang, H. & Huang, W. Self-supervised contrastive learning achieves 12-lead ecg classification. *Biomed. Signal Process. Control.* **112**, 108420, DOI: <https://doi.org/10.1016/j.bspc.2025.108420> (2026).
32. He, S., Ye, X. & Sakurai, T. Clop-herg: The contrastive learning optimized pre-trained model for representation learning in predicting drug-induced herg channel blockers. *Medinformatics* **1**, 103–111, DOI: <https://doi.org/10.47852/bonviewMEDIN42022049> (2024).
33. Moody, G. A new method for detecting atrial fibrillation using rr intervals. *Proc. Comput. Cardiol.* **10**, 227–230, DOI: <https://www.physionet.org/content/afdb/1.0.0/> (1983).
34. Wang, X. *et al.* Paroxysmal atrial fibrillation events detection from dynamic ecg recordings: The 4th china physiological signal challenge 2021. *Proc. PhysioNet* 1–83, DOI: <https://physionet.org/content/cpsc2021/1.0.0> (2021).
35. Anbalagan, T., Nath, M. K., Vijayalakshmi, D. & Anbalagan, A. Analysis of various techniques for ecg signal in healthcare, past, present, and future. *Biomed. Eng. Adv.* **6**, 100089, DOI: <https://doi.org/10.1016/j.bea.2023.100089> (2023).
36. Attia, Z. I. *et al.* An artificial intelligence-enabled ecg algorithm for the identification of patients with atrial fibrillation during sinus rhythm: a retrospective analysis of outcome prediction. *The Lancet* **394**, 861–867, DOI: [https://doi.org/10.1016/S0140-6736\(19\)31721-0](https://doi.org/10.1016/S0140-6736(19)31721-0) (2019).

37. Zhao, Z. & Zhang, Y. Sqi quality evaluation mechanism of single-lead ecg signal based on simple heuristic fusion and fuzzy comprehensive evaluation. *Front. physiology* **9**, 727, DOI: <https://doi.org/10.3389/fphys.2018.00727> (2018).

38. Makowski, D. *et al.* Neurokit2: A python toolbox for neurophysiological signal processing. *Behav. research methods* **53**, 1689–1696, DOI: <https://github.com/neuropsychology/NeuroKit> (2021).

39. Oppenheim, A. V. *Discrete-time signal processing* (Pearson Education India, 1999).

40. Cho, K. *et al.* Learning phrase representations using rnn encoder-decoder for statistical machine translation. *arXiv preprint arXiv:1406.1078* (<https://doi.org/10.48550/arXiv.1406.1078>).

41. Khosla, P. *et al.* Supervised contrastive learning. *Adv. neural information processing systems* **33**, 18661–18673, DOI: <https://doi.org/10.48550/arXiv.2004.11362> (2020).

42. Adam, J. D. B. J. *et al.* A method for stochastic optimization. *arXiv preprint arXiv:1412.6980* **1412**, DOI: <https://doi.org/10.48550/arXiv.1412.6980> (2014).

43. Selvaraju, R. R. *et al.* Grad-cam: Visual explanations from deep networks via gradient-based localization. In *Proceedings of the IEEE international conference on computer vision*, 618–626, DOI: <https://doi.org/10.1109/ICCV.2017.74> (2017).

44. Cinotti, E. *et al.* An edge ai approach for low-power, real-time atrial fibrillation detection on wearable devices based on heartbeat intervals. *Sensors* **25**, 7244, DOI: <https://doi.org/10.3390/s25237244> (2025).

45. Abdelrazik, A. *et al.* Wearable devices for arrhythmia detection: advancements and clinical implications. *Sensors (Basel, Switzerland)* **25**, 2848, DOI: <https://doi.org/10.3390/s25092848> (2025).

46. Singh, O. & Sunkaria, R. K. Ecg signal denoising via empirical wavelet transform. *Australas. physical & engineering sciences medicine* **40**, 219–229, DOI: <https://doi.org/10.1007/s13246-016-0510-6> (2017).

47. Singh, O. & Sunkaria, R. K. Powerline interference reduction in ecg signals using empirical wavelet transform and adaptive filtering. *J. medical engineering & technology* **39**, 60–68, DOI: <https://doi.org/10.3109/03091902.2014.979954> (2015).